Key Points:
- Most GCMs consider radiation with suspended cloud
- We characterize the radiation impacts of snow in CGCMs
- The impacts of snow-radiation are significant

Correspondence to:
J.-L. F. Li,
Juilin.F.Li@jpl.nasa.gov

Considering the radiative effects of snow on tropical Pacific Ocean radiative heating profiles in contemporary GCMs using A-Train observations

J.-L. F. Li[1], Wei-Liang Lee[2], Duane Waliser[1], Yi-Hui Wang[1], Jia-Yuh Yu[3], Xianan Jiang[4], Tristan L'Ecuyer[5], Yi-Chun Chen[1], Terry Kubar[4], Eric Fetzer[1], and M. Mahakur[6]

[1]Jet Propulsion Laboratory, California Institute of Technology, Pasadena, California, USA, [2]RCEC, Academia Sinica, Taipei, Taiwan, [3]Department of Atmospheric Sciences, National Central University, Taoyuan City, Taiwan, [4]Joint Institute for Regional Earth System Science and Engineering, University of California, Los Angeles, California, USA, [5]Department of Atmospheric and Oceanic Sciences, University of Wisconsin-Madison, Madison, Wisconsin, USA, [6]Indian Institute of Tropical Meteorology, Pune, India

Abstract This study characterizes biases in water vapor, dynamics, shortwave (SW) and longwave (LW) radiative properties in contemporary global climate models (GCMs) against observations over tropical Pacific Ocean. The observations are based on Atmospheric Infrared Sounder for water vapor, CloudSat 2B-FLXHR-LIDAR for LW and SW radiative heating profiles, and radiative flux from Clouds and the Earth's Radiant Energy System products. The model radiative heating profiles are adopted from the coupled and uncoupled National Center for Atmospheric Research (NCAR) Community Earth System Model version 1 (CESM1) and joint Year of Tropical Convection (YOTC)/Madden Julian Oscillation (MJO) Task Force-Global Energy and Water Cycle Experiment Atmospheric System Studies (GASS) Multi-Model Physical Processes Experiment (YOTC-GASS). The results from the model evaluation for YOTC-GASS and NCAR CESM1 demonstrate a number of systematic radiative biases. These biases include excessive outgoing LW radiation and excessive SW surface radiative fluxes, in conjunction with a radiatively unstable atmosphere with excessive LW cooling in the upper troposphere over convectively active areas, such as the Intertropical Convergence Zone/South Pacific Convergence Zone (ITCZ/SPCZ) and warm pool. Using sensitivity experiments with the NCAR-uncoupled/NCAR-coupled CESM1, we infer that these biases partly result from the interactions between falling snow and radiation that are missing in most contemporary GCMs (e.g., YOTC-GASS, Coupled Model Intercomparison Project 3 (CMIP)3, and Atmospheric Model Intercomparison Project 5 (AMIP5)/CMIP5). A number of biases in the YOTC-GASS model simulations are consistent with model biases in CMIP3, AMIP5/CMIP5, and NCAR-uncoupled/NCAR-coupled model simulation without snow-radiation interactions. These include excessive upper level convection and low level downward motion with outflow from ITCZ/SPCZ. This generates weaker low-level trade winds and excessive precipitation in the Central Pacific Trade wind regions. The excessive LW radiative cooling in NCAR-coupled/NCAR-uncoupled GCM simulations is reduced by 10–20% with snow-radiative effects considered.

1. Introduction

The uncertainty of representing clouds, precipitating hydrometeors, and their radiative impacts on hydrological feedback processes is still the largest weakness of current coupled global climate models (CGCMs) [*Stephens*, 2005; *Randall et al.*, 2007; Intergovernmental Panel on Climate Change assessments Fifth Assessment Report (IPCC AR5): http://www.climatechange2013.org]. It has been reported that current CGCMs exhibit systematic radiation biases, which include excessive top of atmosphere (TOA) outgoing longwave radiation (RLUT) and overestimated downward shortwave radiation at the surface over heavy precipitation regions such as the western Pacific, midlatitude storm tracks, and Intertropical Convergence Zone (ITCZ) [e.g., *Li et al.*, 2013, 2014a, 2014b]. As Figure 1 shows, the excessive TOA RLUT biases are present in these regions with values on the order of 5–$20\,\mathrm{W\,m^{-2}}$ for Atmospheric Model Intercomparison Project 5 (AMIP5) and Coupled Model Intercomparison Project 5 (CMIP5) (reproduced from *Li et al.* [2013]) against the Clouds and the Earth's Radiant Energy System-Energy Balanced and Filled (CERES-EBAF) [*Loeb et al.*, 2012, 2009] observations. These radiation biases are found to be closely linked to the biases in ocean surface such as the excessive rainfall within the tropical Pacific trade wind regions [*Li et al.*, 2014c, 2015]. All of these radiation biases are fairly common in terms of pattern and amplitude; similar to each other in
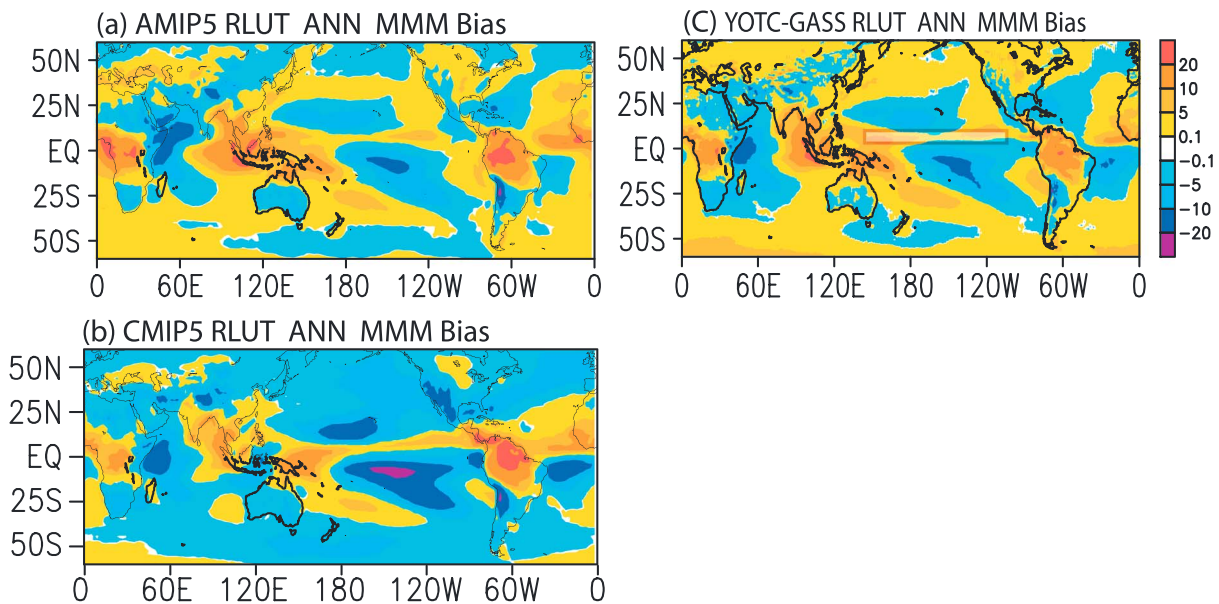
Figure 1. (a) The annual mean (ANN) map of biases for fluxes of radiative longwave upward at the top of the atmosphere (RLUT: W m^{-2}) from the twentieth century (1979–2005) AMIP5 GCM multimodel mean (MMM) against the CERES-EBAF (2003–2010); (b) same as Figure 1a but for CMIP5 MMM; (c) same Figure 1a but for the annual mean maps of radiation flux biases (W m^{-2}) from the twentieth century (1991–2010) YOTC-Task Force GASS MMM AMIP runs against the CERES-EBAF annual mean (2003–2010).

the state-of-the-art CGCMs, such as those in CMIP3/CMIP5 models; and are partially attributable to the missing (or improper) representation of precipitating hydrometeors (i.e., snow) and their radiative effects [e.g., *Li et al.*, 2013, 2014a, 2014b].

Li et al. [2014a], for example, studied the sensitivity of a number of variables to the cloud snow radiative effect using National Center for Atmospheric Research (NCAR) Community Earth System Model version 1 (CESM1). They concluded that radiative flux biases in the Tropical Pacific deep convective regions, resulted from excluding the snow-radiation effect, occur in conjunction with enhanced subsidence north of the SPCZ and south of the Pacific ITCZ (referred to as a V-shaped region shown in Figure 4b of *Li et al.* [2015]). Corresponding to the absence of the snow-radiation effect, weaker surface wind speeds, declined surface wind mixing, and warmer SSTs are observed in the V-shaped regions.

However, the surface and TOA radiation biases and their manifestations in vertical radiative heating rates and their associated precipitation, circulation, and dynamics have not been fully characterized and understood due to the lack of available radiative heating rates in CMIP model output. It is fortunate that a new data set, providing the vertical radiative heating output for uncoupled simulations from the Year of Tropical Convection (YOTC)/ Madden Julian Oscillation (MJO) Task Force-Global Energy and Water Cycle Experiment (GEWEX) Atmospheric System Studies (GASS) Multi-Model Physical Processes Experiment (YOTC-GASS) atmospheric global circulation models (AGCMs) [*Jiang et al.*, 2015], allows us to further quantify the biases of the radiative heating rates in state-of-the-art AGCMs commonly used in CMIP5/AMIP5 against the CloudSat-CALIPSO-derived 2B-FLXHR-LIDAR radiative heating profiles. Examining the biases in the vertical radiative heating of this new data set will advance our understanding of previous studies and shed more light on the link between the radiation and the associated cloud condensational heating by isolating the influences from the ocean related processes.

One of our main goals is to characterize the GCM biases in radiative heating rates, along with biases in winds, water vapor, and cloud mass by utilizing simulations from the YOTC-GASS [*Jiang* et al., 2014]. We conduct in-depth analysis to understand the relationships underlying the cloud-precipitation-water vapor-radiation interactions in 14 YOTC-GASS "conventional" GCMs against observations. Conventional atmospheric GCMs are defined here as those that only have prognostic floating ice/liquid with horizontal resolution larger than 100 km, listed in Table 1 (and in *Jiang et al.* [2015] with the corresponding references). The GCMs excluded in this study are SPCCSM, EC_CEM, MPI_ECHAM6-Coupled GCM, NRL_NAVGEv1.0, CNRM_CGCM, ISUGCM, and SMHI_ecearth3 (with asterisk in Table 1).

Table 1. Participating YOTC-GASS/MJOTF Models With Horizontal/Vertical Resolutions

Models	Institutes	Hori. Resolution (Longitude × Latitude), Vertical Levels	References
1. NASA GMAO GEOS5	Global Modeling and Assimilation Office, NASA	0.625° × 0.5°, L72	*Molod et al.* [2012]
2. SPCCSM[a]	George Mason University	T42 (2.8°), L30	*Stan et al.* [2010]
3. GISS_ModelE2	Goddard Institute for Space Studies, NASA	2.5° × 2.0°, L40	*Schmidt et al.* [2014]
4. EC_CEM[a]	Environment Canada	1.4°, L64	*Côté et al.* [1998]
5. MIROC5	AORI/NIES/JAMSREC, Japan	T85 (1.5°), L40	*Watanabe et al.* [2010]
6. MRI-AGCM	Meteorological Research Institute, Japan	T159, L48	*Yukimoto et al.* [2012]
7. CWB_GFS	Central Weather Bureau, Taiwan	T119 (1°), L40	*Liou et al.* [1997]
8. MPI_ECHAM6-Coupled GCM	Max Planck Institute for Meteorology	T63 (2°), L47	*Stevens et al.* [2013]
9. NCAR_CAM5	National Center for Atmospheric Research	1.25° × 0.9°, L30	*Neale et al.* [2012]
10. NRL_NAVGEMv1.0[a]	U.S. Naval Research Laboratory	T359 (37 km), L42	Not available; differs from NAVGEM 1.1 [*Hogan et al.*, 2012]
11. UCSD_CAM	Scripps Institute of Oceanography	T42 (2.8°), L26	*Zhang and Mu* [2005]
12. CNRM_AM	Centre National de la Recherche Scientifique/Météo-France	T127 (1.4), L31	*Voldoire et al.* [2013]
13. CNRM_CM[a]	Centre National de la Recherche Scientifique/Météo-France	T127 (1.4), L31	*Voldoire et al.* [2013]
14. CNRM_ACM	Centre National de la Recherche Scientifique/Météo-France	T127 (1.4), L31	*Voldoire et al.* [2013]
15. CCCma_CanCM4	Canadian Centre for Climate Modelling and Analysis	2.8°, L35	*Merryfield et al.* [2013]
16. BCC_AGCM2.1	Beijing Climate Center, China Meteorological Administration	T42 (2.8°), L26	*Wu et al.* [2010]
17. FGOALS-s2	Institute of Atmospheric Physics, Chinese Academy of Sciences	R42 (2.8° × 1.6°), L26	*Bao et al.* [2013]
18. TAMU_M-CAM4	Texas A&M University	2.5° × 1.9°, L26	*Lappen and Schumacher* [2012]
19. MetUM_GA3	U.K. Met Office	1.875° × 1.25°, L85	*Walters et al.* [2011]
20. ISUGCM[a]	Iowa State University	T42 (2.8°), L18	*Wu and Deng* [2013]
21. SMHI_ecearth3[a]	Rossby Centre, Swedish Meteorological and Hydrological Institute	T255 (80 km), L91	*Hazeleger et al.* [2012]; a new cloud microphysics [*Forbes et al.*, 2012].

[a]Models which are not included in this study.

In order to explore and characterize the potential impacts of ignoring precipitating hydrometeors (i.e., snow) on radiation including radiative heating profiles and the atmospheric circulation, we further use the uncoupled and coupled NCAR CAM5 model and conduct AMIP-like (forced by prescribed historical interannual vary SSTs) sensitivity experiments by turning off (hereafter, NoS) and on (hereafter, S) the radiation interaction with snow. That is, the experiments include one simulation without diagnostic snow-radiation interaction and the other with diagnostic snow-radiation interaction. The specific experimental scenario used in the sensitivity experiments is the AMIP5 historical twentieth century simulation (1850 to 2005) which uses the observed twentieth century greenhouse gas, ozone, aerosol, and solar forcing [*Taylor et al.*, 2012]. The simulation time period used in the analyses presented here is 1970–2005.

Following section 1, we describe the observational resources for the radiative heating profiles, derived radiative fluxes, water vapor, and precipitation used in section 2. In section 3, we briefly describe the model simulations utilized in this study. In section 4, we discuss the results of our study, with summary and conclusions drawn in section 5.

2. Data Source

2.1. Observed Radiative Data Sets

The 2B-FLXHR-LIDAR flux and heating rate algorithm [*L'Ecuyer et al.*, 2008; *Henderson et al.*, 2013] makes use of liquid and ice water content estimates from the CloudSat cloud profiling radar (CPR) [*Austin and Stephens*, 2001; *Austin et al.*, 2009] to produce estimates of broadband fluxes and heating rates at the high spatial and vertical resolution of the radar. The 2B-FLXHR-LIDAR also incorporates measurements from CALIPSO and Moderate Resolution Imaging Spectroradiometer (MODIS) to provide properties of clouds and aerosols undetected by CloudSat. For a particular radar profile, upwelling and downwelling longwave (LW) and shortwave (SW) flux profiles are calculated at discrete levels of the atmosphere using a two-stream radiative transfer model. The corresponding heating rates are computed from the implied vertical convergence or divergence of these fluxes. Profiles of cloud liquid water content (LWC) and effective radius are obtained from
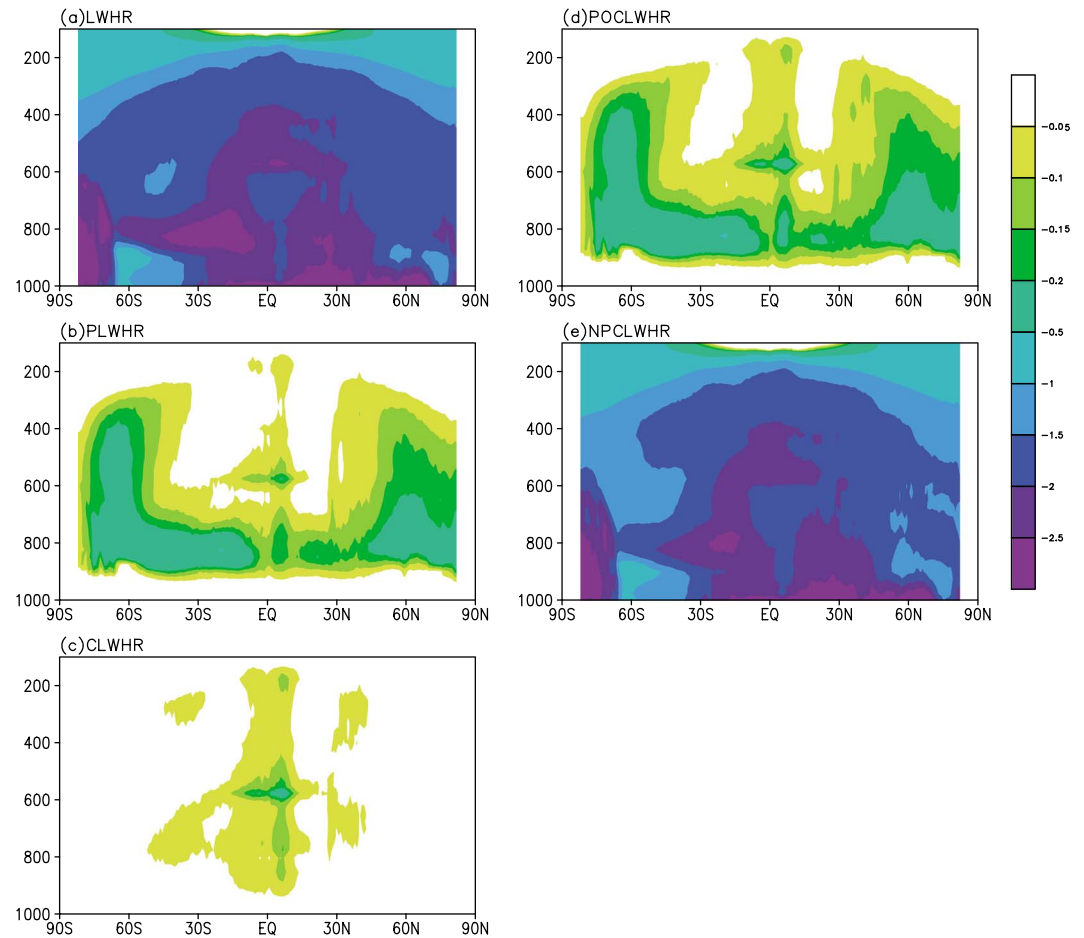
Figure 2. (a) Zonal-average annual mean total longwave heating rates (LWHR; K d^{-1}) from the A-Train/CloudSat 2B-FLXHR-LIDAR product; (b) the same as Figure 2a but filtered according to precipitating conditions (PLWHR) based on CloudSat rain/profile flags; (c) same as Figure 2b but for convective cloud cases only (CLWHR); (d) the same as Figure 2b but filtered out according to precipitating and/or convective conditions (POCLWHR) based on CloudSat cloud classification and rain flags; (e) same as in Figure 2b but for nonprecipitating and nonconvective cloud cases only (NPCLWHR). Units: K d^{-1}.

the CloudSat 2B-LWC product. CloudSat LWC estimates are known to be adversely impacted by the presence of drizzle or precipitation in the column. This is addressed in 2B-FLXHR-LIDAR by assigning liquid water content and particle size based on the 2C-PRECIP-COLUMN product in all profiles that are believed to contain precipitation [*Haynes et al.*, 2009]. In such profiles, a Marshall-Palmer size distribution is assumed to describe raindrops, and this is augmented by an estimate of cloud water content consistent with field observations of warm rain clouds that is distributed among 50 μm cloud droplets. Ice water content and ice particle effective radii are obtained from the CloudSat 2B-ice water content (IWC) product. Scattering properties of ice are defined using temperature-dependent scattering models described in *Austin et al.* [2009]. (Details are in http://www.cloudsat.cira.colostate.edu/data-products/level-2b/2b-flxhr-lidar.) Ice water content profiles that include both cloud and precipitating ice are supplied by 2B-IWC. The LWC and IWC of clouds found in the CALIPSO CAL_LID_L2_05kmCLay that are not detected by CloudSat are estimated from optical depths reported by CloudSat's MODIS-based 2B-Tau product or inferred from Cloud-Aerosol Lidar with Orthogonal Polarization (CALIOP) backscatter observations. Aerosol location, optical depth, and single-scatter properties are obtained by coupling CALIPSO's CAL_LID_L2_05kmALay product to optical property models adopted in the Spectral Radiation Transport Model for Aerosol Species (SPRINTARS) [*Takemura et al.*, 2002]. All other atmospheric state variables including temperature, humidity, and ozone are obtained from ECMWF analyses and surface albedos are prescribed using seasonally varying maps of surface reflectance properties derived from the International Geosphere-Biosphere Program. For additional detail regarding the theoretical basis
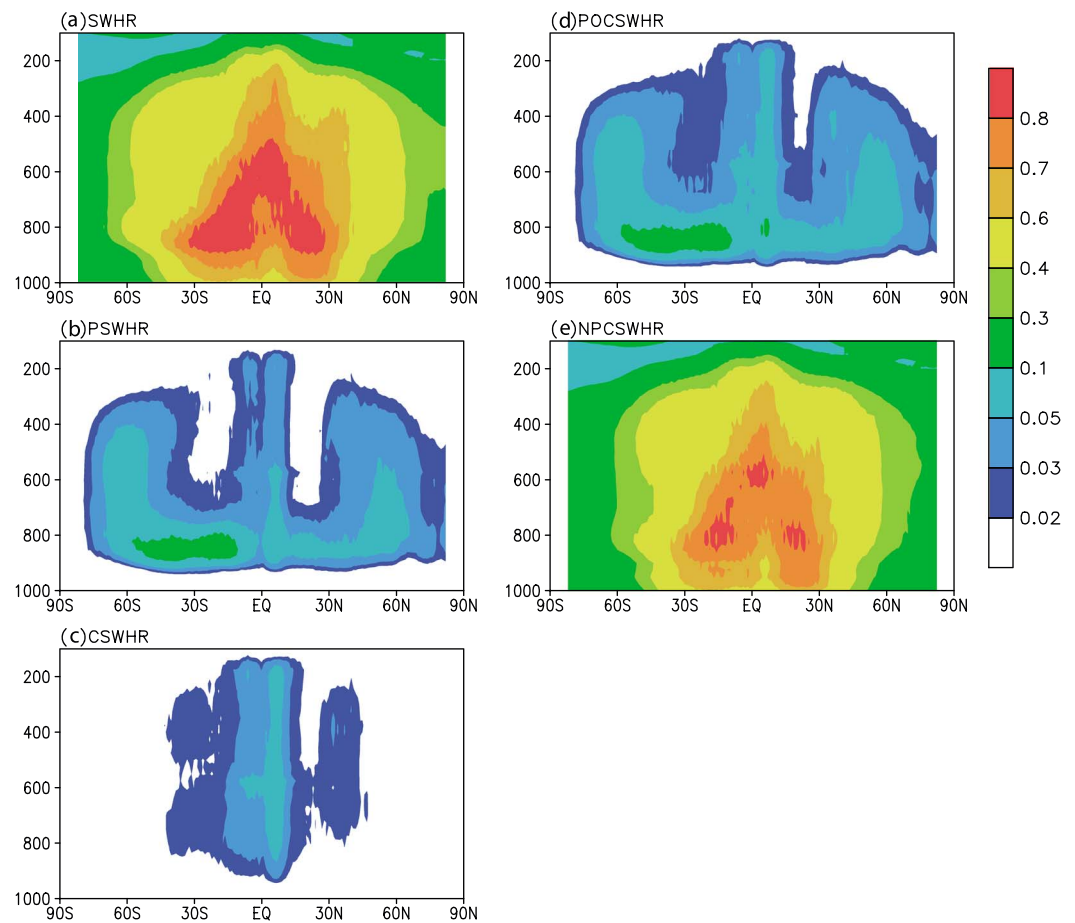
Figure 3. (a) Zonal-average annual mean total shortwave heating rates (SWHR; $K d^{-1}$) from the A-Train/CloudSat 2B-FLXHR-LIDAR product (see text); (b) the same as Figure 3a but filtered according to precipitating conditions (PSWHR) based on CloudSat rain flags; (c) same as in Figure 3b but for convective cloud cases only (CSWHR); (d) the same as Figure 3b but filtered according to precipitating and/or convective conditions (POCSWHR) based on CloudSat cloud classification and rain flags; (e) same as in Figure 3b but for nonprecipitating and nonconvective cloud cases only (NPCSWHR). Units: $K d^{-1}$.

of the 2B-FLXHR-LIDAR algorithm and all relevant input and output specifications, please see *L'Ecuyer et al.* [2008] and *Henderson et al.* [2013].

In order to have a meaningful model observation heating rate comparison for models which do not include precipitating and convective cloud masses in their radiative heating rate calculations, the convective and precipitating ice/liquid mass should be removed from the satellite-derived values of SW/LW radiative heating rates. The approach used to distinguish ice mass associated with clouds from ice mass associated with precipitation and convection based on CloudSat cloud classification and rain flags is referred to here as the FLAG method [*Li et al.*, 2008, 2012; *Waliser et al.*, 2009]. This method has been previously used in model-data comparisons for IWC in many studies [e.g., *Li et al.*, 2008, 2012; *Waliser et al.*, 2009; *Gettelman et al.*, 2010; *Song et al.*, 2012].

Radiative heating rates associated with cloudy, precipitating and convective conditions are shown in Figure 2 for LWHR and Figure 3 for SWHR. Illustrated in Figures 2 and 3 are zonally averaged annual mean (2007–2012) total LW and SW heating rates (Figure 2a: LWHR; Figure 3a: SWHR) as a function of height and latitude, respectively. Following *Li et al.* [2011], all the retrievals in any profile that are flagged as precipitating at the surface (based on precipitation flag defined from CloudSat 2B-CLDCLASS data) are defined as precipitating LW and SW heating rates (Figure 2b: PLWHR; Figure 3b: PSWHR), and any retrieval within the profile whose cloud type is classified as "deep convection" or "cumulus" from CloudSat 2B-CLDCLASS data is referred to as convective LW and SW heating rates, shown in Figures 2c (CLWHR) and 3c (CSWHR). The combination of these conditions, i.e., precipitation and/or convective, i.e., PLWHR and/or CLWHR, is referred to as POCLWHR and

POCSWHR and are shown in Figures 2d and 3d, respectively. An estimate of the cloud-only portion of the LWHR and SWHR (hereafter, referred to as NPCLWHR and NPCSWHR, respectively) are shown in Figures 2e and 3e. For more details, please see *L'Ecuyer et al.* [2008] and *Henderson et al.* [2013].

The overall vertical-meridional structure of total LWHR (Figure 2a) exhibits four local cooling maxima; one in the deep tropics near 500 hPa, one over the Antarctic, and the other two at 1000 and 800 hPa in the midlatitudes of the Southern and Northern Hemispheres, respectively, corresponding to the subsiding braches of the Hadley circulation.

The most up-to-date TOA Radiative Longwave Upward (RLUT) and Radiative Shortwave Upward (RSUT) fluxes are available from the CERES Energy Balanced and Filled (EBAF) product (CERES_EBAF-TOA_Ed2.6r) [*Loeb et al.*, 2012, 2009]. The CERES EBAF product includes the latest instrument calibration improvements, algorithm enhancements, and other updates. CERES TOA SW and LW fluxes in the EBAF product are used for average global TOA flux in this study.

2.2. AIRS: Specific Humidity Profile

The water vapor measurements used in this study are specific humidity from the Atmospheric Infrared Sounder (AIRS) Level 3 (L3) version 6 (V6) standard monthly products [*Tian et al.*, 2013b]. The AIRS L3 products used here are monthly averaged, gridded level 2 (L2) retrievals [*Olsen et al.*, 2013] of specific humidity profiles with $1° \times 1°$ horizontal resolution. Moreover, as the AIRS water vapor measurements do not have sensitivity above about 300 hPa [*Fetzer et al.*, 2008] and our study is mainly focused on tropospheric effects, we only use the AIRS L3 specific humidity on the lowest eight pressure levels (1000, 925, 850, 700, 600, 500, 400, and 300 hPa). The time period of the observational data used in this study is from January 2003 to December 2010.

2.3. Precipitation

The long-term mean precipitation is obtained from the Global Precipitation Climatology Project (GPCP) [*Huffman et al.*, 1997]. As it is a merging of several satellite observations (e.g., infrared and microwave) and in situ measurements, it is representative of the late twentieth century.

2.4. Reanalysis References

The dynamical fields are from the European Centre for Medium-Range Forecasts (ECMWF)-Interim reanalysis [*Dee and Uppala*, 2009] and can be downloaded at http://www.ecmwf.int/products/data/archive/descriptions/ei/.

3. Modeled Values

3.1. YOTC-GASS GCMs

Note that the CMIP3 and CMIP5 twentieth century model output does not include vertical profiles of radiative heating rates. Instead, we take advantage of recent climate simulations from the joint multimodel project organized by the Year of Tropical Convection (YOTC) activity, GEWEX Global Atmospheric System Studies (GASS), and Madden Julian Oscillation Task Force (MJOTF) [*Petch et al.*, 2011; *Jiang et al.*, 2015], which will be referred to here as the YOTC-GASS experiment. Using the observations described in the previous section, we evaluate the biases in YOTC-GASS GCMs.

We analyze 14 atmospheric GCMs output from the 20 year climatological simulation component of the YOTC-GASS experiment [*Jiang et al.*, 2015]. The climate simulations from this project provide model output every 6 h, mapped to a spatial resolution of 2.5° latitude by 2.5° longitude, over 22 pressure levels from 1000 hPa to 50 hPa. All the selected YOTC/MJOTF-GASS simulations shown in Table 1 utilized specified sea surface temperature (SST).

3.2. NCAR CESM1 Coupled Model and Sensitivity Experiments

The NCAR Community Earth System Model (CESM) is a coupled climate model for simulating Earth's climate system. Composed of four separate models that simultaneously simulate Earth's atmosphere, ocean, land surface, and sea ice, and one central coupler component, the CESM allows researchers to conduct fundamental research into the Earth's past, present, and future climate states (model code and documentation available from http://www.cesm.ucar.edu/models/cesm1.0/). This study uses uncoupled/coupled NCAR CESM1 and contains options of the CAM5 [*Morrison and Gettelman*, 2008; *Neale et al.*, 2012]. The CAM5 physics account
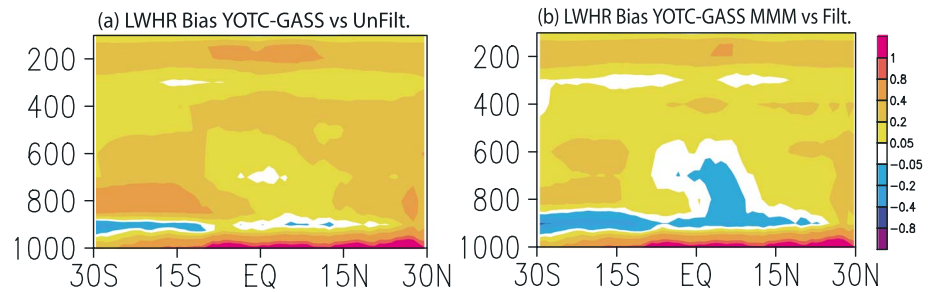
Figure 4. (a) Zonally averaged annual mean biases of YOTC-GASS models in total longwave heating rates (LWHR; $K d^{-1}$) against the A-Train/CloudSat 2B-FLXHR-LIDAR product (shown in Figure 2a); (b) the same as Figure 4a but against non-precipitating and nonconvective cloud cases only (NPCLWHR shown in Figure 3e). Units: $K d^{-1}$.

for and include cloud microphysics, radiative transfer, macrophysics, aerosol formation, ice clouds, and shallow convection, in addition to a new moist turbulence parameterization. Snow in the model represents falling large ice crystals with appreciable fall velocities that are diagnosed from falling ice mass flux profiles at each model level and every model physical time step. Because CAM5 incorporates the impact of snow on radiative fluxes, it is suitable for the objectives of this study [*Li et al.*, 2012, 2013, 2014a, 2014b]. Details of the performance of the cloud-related physical parameterizations can be found in *Morrison and Gettelman* [2008], *Gettelman et al.* [2010], *Lindvall et al.* [2013], and many others.

The experiments include one simulation without the diagnostic snow-radiation effect (hereafter, NoS), and another with diagnostic cloud snow-radiation interaction (hereafter, S). The sensitivity of model fields to the snow in the radiative calculations is calculated as the difference of the simulation with the snow-radiative effect off minus the simulation with snow-radiative effect on, which is referred to as NoS-S. Both simulations are set up in the same manner as that used in the AMIP5.

The specific experimental scenario used in the sensitivity experiment is based on the AMIP5 historical twentieth century simulation (1850 to 2005), which uses the observed twentieth century greenhouse gas, ozone, aerosol, and solar forcing [*Taylor et al.*, 2012]. The simulation time period used in the analyses here is 1970–2005. For the purposes of comparison, both the GCM and observational data sets are regridded onto a common horizontal resolution of 4° latitude by 5° longitude.

4. Results

4.1. Radiation Biases

In comparison with the biases in AMIP5 (Figure 1a) and CMIP5 (Figure 1b), Figure 1c shows the biases of annual mean of RLUT from the multimodel mean (MMM) of the YOTC-GASS simulations as well as from the uncoupled CESM1 (not shown) sensitivity experiments against the CERES-EBAF data. Common features are present across models, including excessive downward SW radiation at the surface (not shown) and LW emission to space at TOA, particularly in areas with high cloud coverage. It has been suggested that such biases might be due to the fact that models do not include the influence of falling and/or convective core hydrometeors on radiation in the western Pacific, ITCZ/SPCZ, tropical landmass and storm tracks [*Li et al.*, 2013, 2014a, 2014b; *Waliser et al.*, 2011].

4.2. Biases of the Vertical Structure of Radiation in YOTC-GASS

Figure 4 shows the biases in the YOTC-GASS MMM simulations for the zonally averaged LWHR ($K d^{-1}$) with warming in the lower levels against observed total LW cooling rates (Figure 2a) and observed LW cooling rate for nonprecipitating and nonconvective cases (referred to as cloud only, shown in Figure 3e) for the deep tropics (30°S ~ 30°N). Both indicate an overestimate of LW cooling with too strong low-level radiative cooling near 900 hPa.

As shown in Figure 4b, overestimates of LW cooling between 900 and 700 hPa exist over the northern subtropics against cloud only observed estimated LW cooling rates. The biases are smaller compared to the total (i.e., cloud and snow) LW cooling rates estimates, including all particles (Figure 4a), due to the fact that models do not consider the snow radiative effects. These modeled LWHR compared to cloud only values indicate
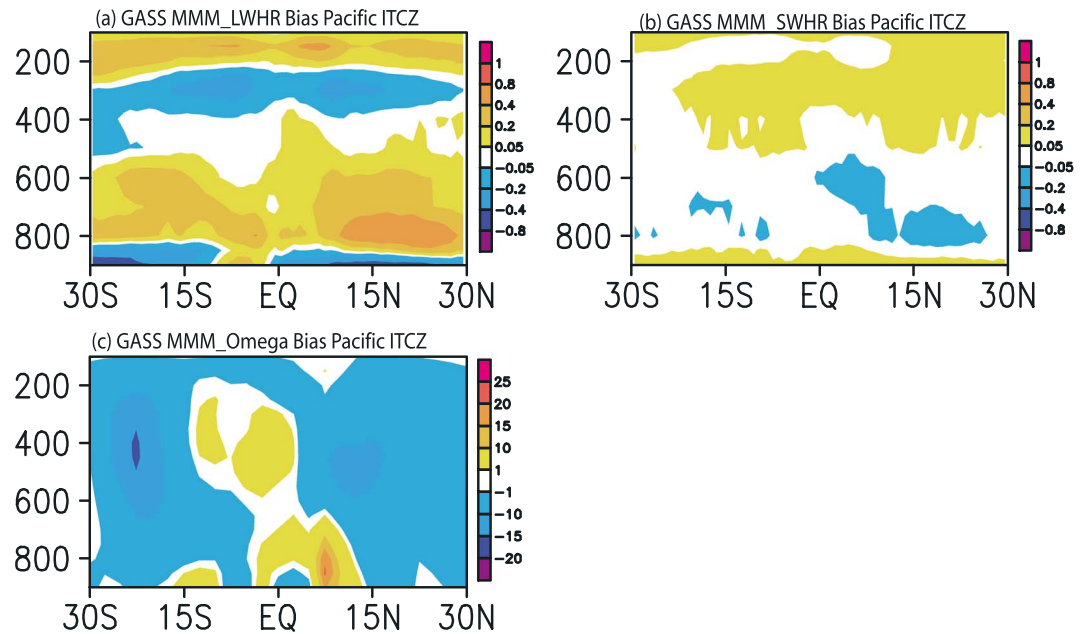
Figure 5. Zonally averaged annual mean biases from multimodel mean (MMM) between 180°W to 80°W for vertical profiles of (a) longwave (LW) heating rates (LWHR; K d^{-1}); (b) shortwave heating rates (SWHR; K d^{-1}) for YOTC-MJO Task Force GCMs against CloudSat-CALIPSO-derived 2B-FLXHR-LIDAR. (c) Same as Figure 5a but for profiles of upward motion (negative values) against ECMWF-Interim (Pa/h).

smaller biases consistent with the IWC model-data comparisons due to the fact that models only consider floating cloud for cloud radiative heating effects (i.e., no snow-radiative effects considered in the models).

In the following, we explore the GCM biases of winds, water vapor, and cloud mass, and to thoroughly understand the nature of the radiative heating rates with a focus on the deep tropics over the Pacific [30°S–30°N; 120°E–60°W], covering western Pacific, and ITCZ/SPCZ. The analysis of global and other specific regions will be reported in other papers.
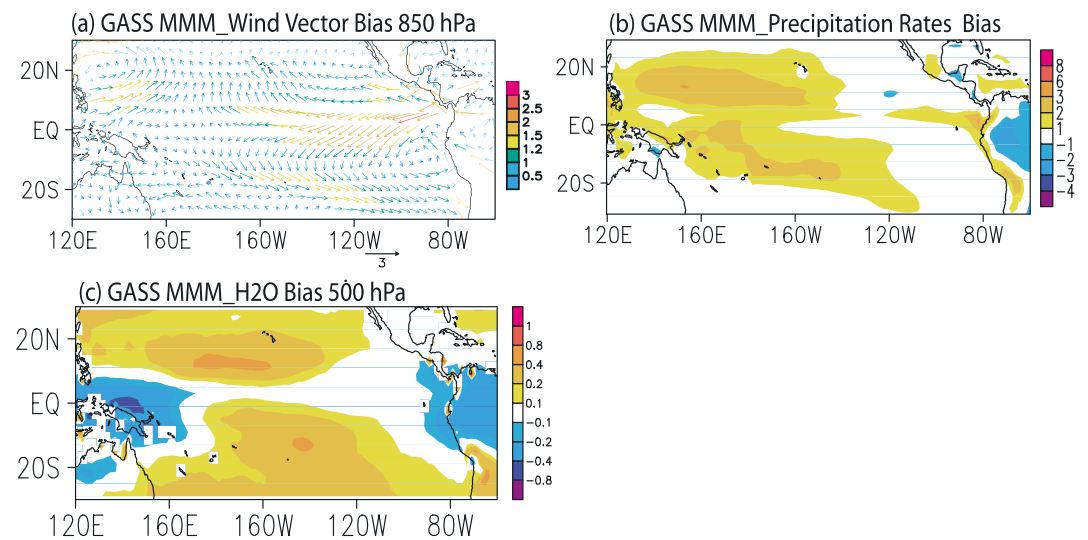
Figure 6. (a) Biases of wind vector changes at 850 hPa (units: m s^{-1}) against ECMWF-Interim; (b) same as in Figure 6a but for the biases of the annual mean precipitation rates (PCP; mm d^{-1}) against GPCP and (c) same as in Figure 6a but for the biases of the annual mean specific humidity at 500 hPa against AIRS (H2O; g kg^{-1}) from the twentieth century (1991–2010) simulations from YOTC-MJO Task Force AGCMs with their multimodel mean.
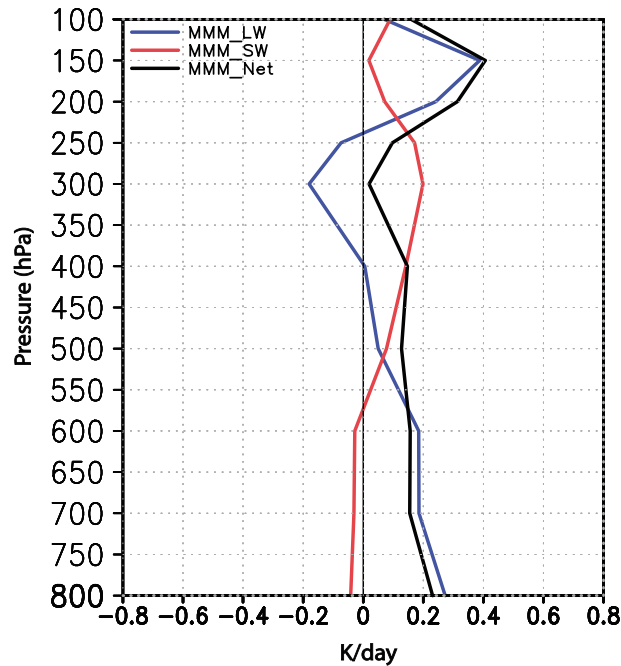
Figure 7. Profiles of annual mean vertical profile biases of shortwave radiative heating rates from multimodel mean (MMM) YOTC-MJO Task Force GASS AGCM (MMM_SW: red), longwave heating rates (MMM_LW: blue), and net heating rates (MMM_Net: black) against CERES-EBAF taken from the brown box region in Figure 1 in the Pacific ITCZ [2°N–12°N; 140°E–100°W] against CloudSat-CALIPSO-derived 2B-FLXHR-LIDAR total radiative heating rates data. Units: (K d^{-1}).

In comparison with observations, the vertical profiles of zonally averaged radiative rate biases in the YOTC-GASS MMM over the central and eastern Pacific (180°W–80°W) in the deep tropics (30°S–30°N) are presented in Figure 5. Biases of the LW radiative cooling rates shown in Figure 5a indicate the upper level overestimation of LW radiative cooling maximizing near 300 hPa over the depth of 300–500 hPa, which is associated with a bias in the vertical ascending motion against ECMWF-Interim data in the northern and southern branches of the ITCZ (~20°S and ~10°N), with maximum biases near 400~500 hPa shown in Figure 5c. In contrast, the LW radiative cooling exhibits a positive bias in the lower troposphere, indicating that there is too little LW cooling relative to observations below 500 hPa in the tropical zone (~30°S to ~30°N). This feature is due to an increase in moisture at 500 hPa (Figure 6c) and total precipitable water (not shown) through "effective" low-level wind transport of moisture from the ITCZ and warm pool to the south and east or weaker trade wind transport from southeast Pacific (Figure 6a). The magnitude of SW heating rate biases is generally smaller relative to its LW cooling counterpart.

Figure 7 shows the LW radiative cooling profile biases for YOTC-GASS for the Pacific ITCZ regions (brown box in Figure 1c) [2°N–12°N; 140°E–100°W] against the 2B-FLXHR-LIDAR total radiative heating rates. The relatively LW radiative warming below ~400 hPa and the relatively LW radiative cooling between ~400 hPa and 250 hPa tend to generate more unstable columns. There is a nontrivial impact (~10–20%) on the vertical tilting of the profiles of net radiative heating, implying that the unstable column is dominated by the vertical structure of LW radiative cooling profile. Note that all the YOTC-GASS GCMs used in this study are uncoupled and do not have snow-radiative effects considered in their radiative transfer calculation. These results are similar to those from the results of coupled GCMs in *Li et al.* [2014a]. *Li et al.* [2014a] reported that the LW radiative cooling/heating profile from the no snow-radiation case produces a temperature tendency that would yield more thermodynamically unstable columns [see *Li et al.*, 2014a, Figure 4]. However, these early studies did not examine the radiative heating structure biases against observations.

4.3. Impacts on Vertical Structure of Radiation and Moist Process in Uncoupled CAM5

In order to explore and characterize the role of snow radiative effect in the above mentioned biases from the *uncoupled* YOTC-GASS GCMs simulations shown in Figures 5, 6, and 7, we use the uncoupled NCAR CAM5 model and conduct AMIP-like (forced by prescribed historical interannual vary SSTs) sensitivity experiments by turning off (NoS) and on (S) the radiation interaction with snow.

The results of the NoS minus S for the zonally-averaged (from 180° to 120°W) LW, SW, net radiative heating rates in terms of K d^{-1} as well as the associated dynamics across the central and eastern Pacific ITCZ are shown in Figure 8. Note that the regional zonal averages especially over the Southern Hemispheric subtropics may be diminished and slightly smoothed due to the anomalies associated with the changes in the vicinity of the southeastward slanted SPCZ.
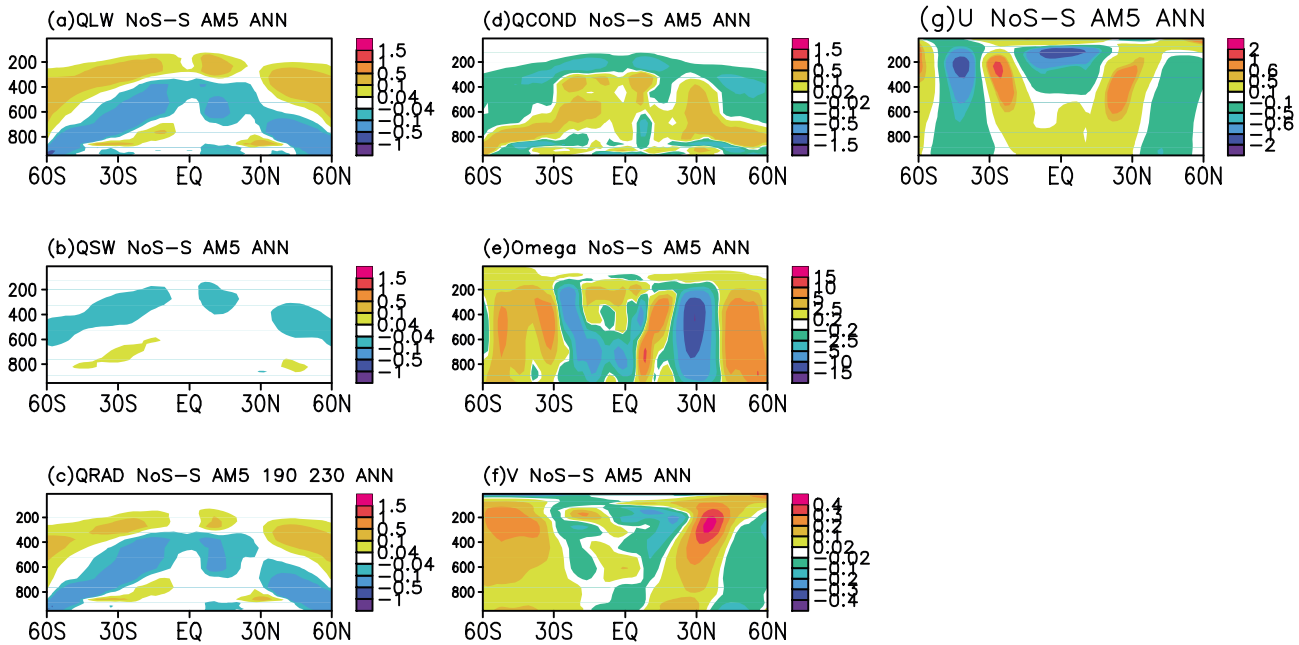
Figure 8. Annual mean changes (snow-radiation off (NoS) minus snow-radiation on (S)) for the zonal-average (from 180°W to 120°W; 60°S to 60°N) (a) vertical longwave (LW) heating rates (QLW; K d^{-1}); (b) shortwave heating (QSW; K d^{-1}); (c) net radiative heating rates (QRAD; K d^{-1}); (d) moist diabatic heating rates (QCOND; K d^{-1}); (e) vertical velocity (Ω; hPa h^{-1}); (f) meridional wind (V; m s^{-1}); and (g) zonal wind (U; m s^{-1}) from the twentieth century (1970–2005) simulations using NCAR CAM5 for the AMIP5 historical run.

The influence of the snow-radiation effect is apparent in both radiative and dynamical variables. Without the presence of snow-radiative effects, there is upper level LW radiative cooling with maximum near 600 hPa and radiative greenhouse warming below 600 hPa in the tropical zone (Figure 8a). The net radiative cooling (Figure 8c) appears to be mainly dependent on the LW cooling (QLW; Figure 8a), in spite of a small contribution from the SW heating (QSW; Figure 8b). This vertical destabilizing radiative gradient leads to the
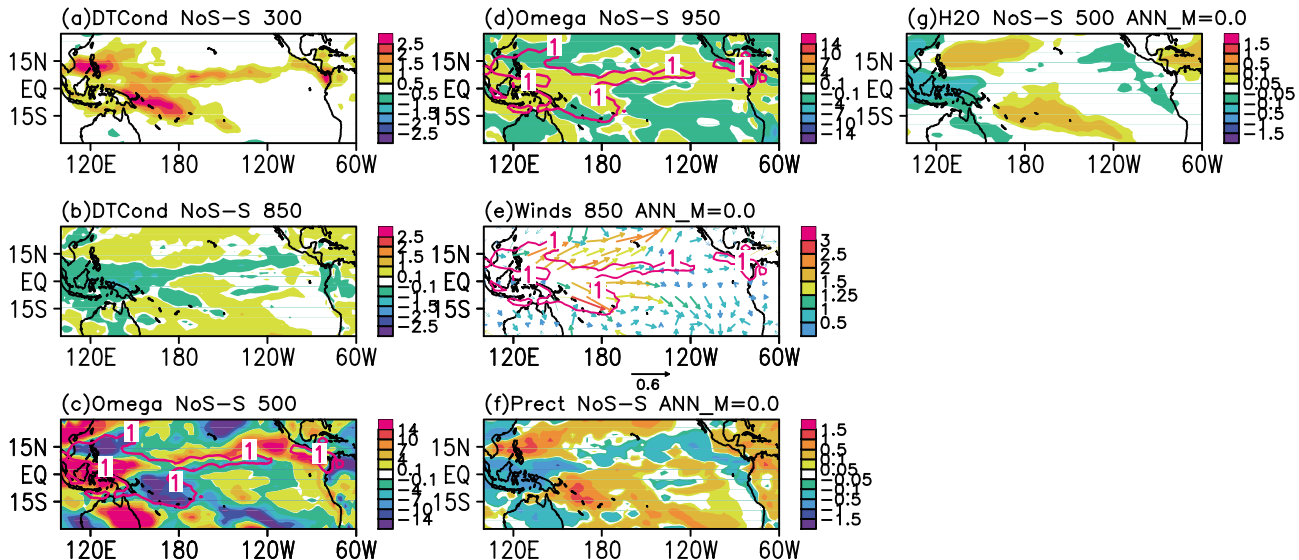
Figure 9. The changes (NoS minus S) of annual mean maps of the following: (a) condensational heating rate at 300 hPa (K d^{-1}); (b) same as Figure 9a but at 850 hPa; (c) vertical upward motion at 500 hPa (Ω; negative for upward motion, unit: Pa h^{-1}); (d) same as Figure 9c but for level at 950 hPa; (e) wind vector changes at the 850 hPa (wind; unit: m s^{-1}). The condensational heating rates is superimposed on Figures 9c–9e in contours for values equal to and greater than the value of 0.25 K; (f) the changes of the precipitation rates (mm d^{-1}); (g) the changes of specific humidity at 500 hPa (H2O; g kg^{-1}) from the twentieth century (1970–2005) simulations using NCAR CAM5 for the AMIP5 historical run.
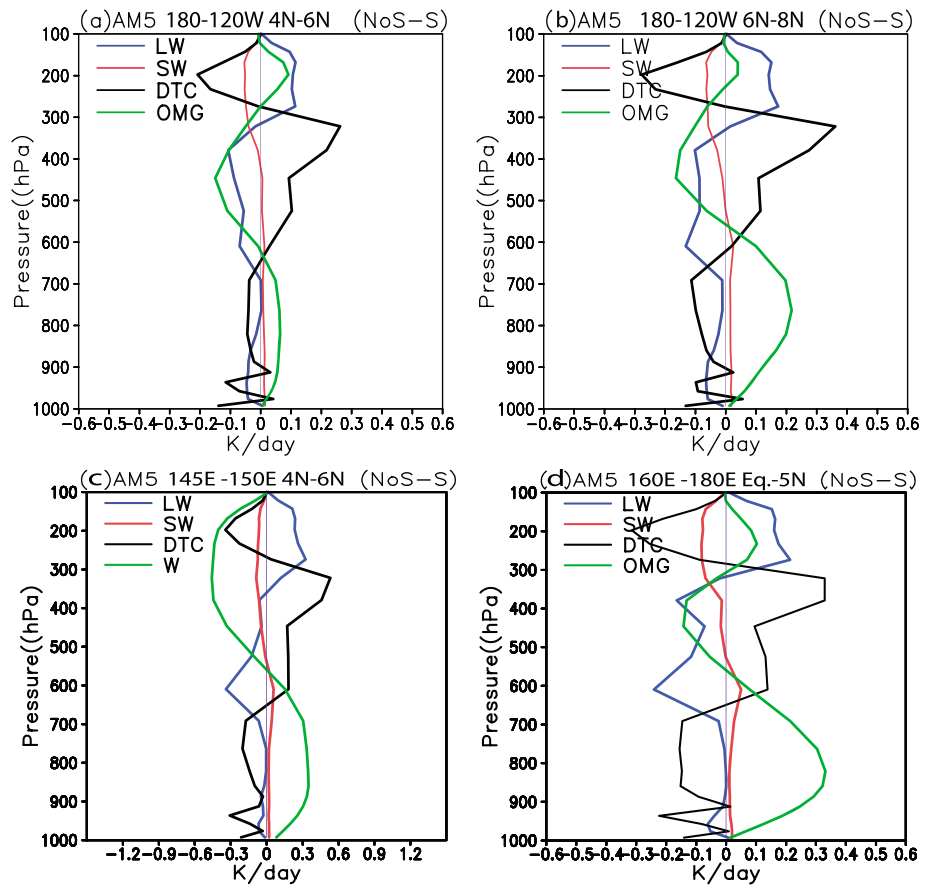
Figure 10. Annual mean differences between a case excluding effects of precipitating snow (NoS) on radiation and the control (S) for (a) shortwave radiative heating rates (red), longwave cooling rate (blue), and the condensational heating rates (black) as well as vertical upward motion (Ω; negative for upward motion, unit: Pa h^{-1}) taken from the region in the central to east Pacific ITCZ [4°N–6°N; 180°–120°W]. (b) The same as in Figure 10a but taken from the region north of the ITCZ [6°N–8°N; 180°–120°W]. (c) The same as in Figure 10a but taken from the region in [4°N–6°N; 145°–150°E]. (d) The same as in Figure 10a but taken from the region in [0°–5°N; 160°–180°E].

compensating deep convective ascending aloft and slightly descending below 600 hPa (Figure 8e), in conjunction with upper level condensational heating (Figure 8d) between 30°S and 5°N with a maximum near 400 hPa. Responding to the low-level subsidence, strengthening meridional divergence near ITCZ (5°N to 8°N) and eastward winds in the tropics is generated (Figures 8f and 8g). The heating difference (NoS-S) indicating the enhanced condensational heating for the NoS (compared to S case) leads to a stronger upper level vertical ascending motion in the north and south branches of the ITCZ. It also indicates greater low-level meridional convergence and upper level divergence with upper level subtropical westerly jets and slight easterly enhancements in the tropics caused by the geostrophic wind adjustment.

The spatial relationship between the changing variables owing to the changing snow-radiation effect is clearly displayed at selected pressure levels. When the snow-radiative effect is not considered, enhanced condensational heating is found in the ITCZ at 300 hPa (Figure 9a), in conjunction with low-level condensational cooling at 850 hPa (Figure 9b). The condensational heating is suggestive of stronger deep convection with more upper level latent heat release. The low-level cooling may be due to rain reevaporative cooling below clouds. As noted above, the anomalous upper level heating and lower level cooling are associated with upward motion aloft (Figure 9c) (associated convective updraft) and downward motion at lower level (Figure 9d) (associated convective downdraft), respectively. Corresponding to the anomalous vertical air motion, there is low-level wind divergence at 850 hPa (Figure 9e), which is consistent with the low-level eastward and southward winds near the ITCZ (~4°N–6°N) shown in Figures 8f and 8g. As a result, low-level moist and warmer air originated from the warm pool and the ITCZ/SPCZ is advected northeastward and southeastward, causing the increased precipitation rates
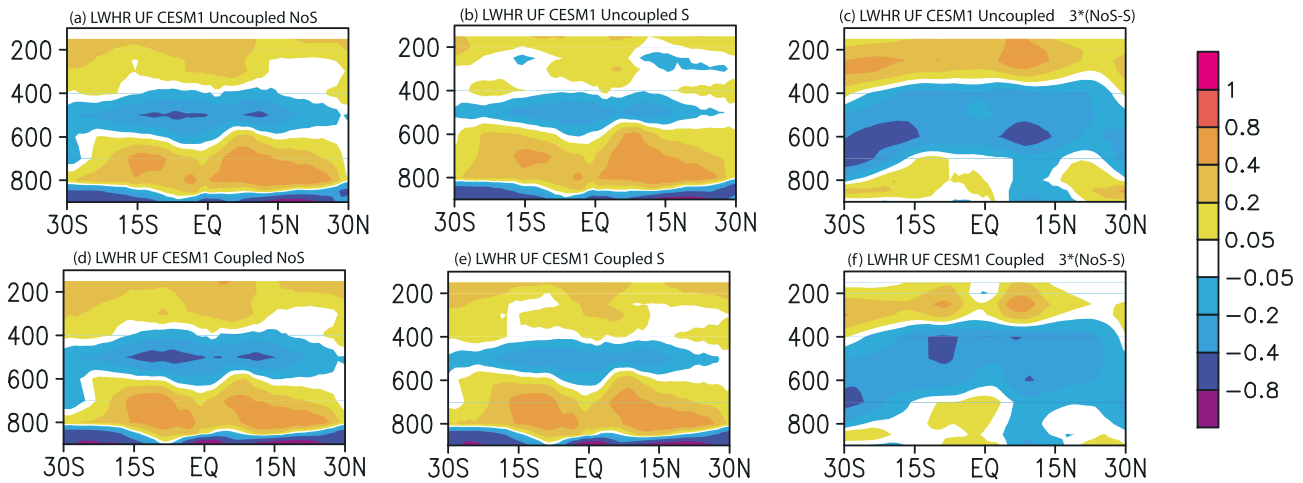
Figure 11. (a) Zonally averaged biases in annual mean longwave radiative cooling rates of NCAR CESM1-CAM5-POP2 for the AMIP5 historical run with snow-radiative effect off (NoS) against CloudSat-CALIPSO derived 2B-FLXHR-LIDAR radiative heating rates data; (b) same as Figure 11a but for the run with snow-radiative effect (S); (d) same as Figure 11a but for CMIP runs; (e) same as Figure 11b but for CMIP run; (c) the zonally averaged annual mean of longwave heating rates for the NoS minus S difference (factor of 3 in units of K d^{-1}) from the twentieth century (1970–2005) simulations using NCAR CESM1-CAM5-POP2 for the AMIP5 historical run; (f) same as Figure 11c but for CMIP run. Units: (K d^{-1}).

(Figure 9f) and water vapor at 500 hPa (Figure 9g) in subtropical regions. The enhanced moisture due to the absence of the snow-radiative effect mitigates the dryness in these subtropical regions which are governed by the trade wind with dry/cold air advection from the cold SSTs regions off the coast of the Peru and California.

To facilitate comparisons, the vertical profiles of the SW, LW, and the condensational heating rates (DTC) as well as vertical upward motion (Ω; negative for upward motion, unit: Pa h^{-1}) for the NoS-S difference over the regions sensitive to the snow radiative effect are displayed together. Figure 10a shows the region in the central to eastern Pacific ITCZ [4°N–6°N; 180°–120°W], while Figure 10b shows the north edge of the ITCZ [6°N–8°N; 180°–120°W]. In spite of the slight meridional displacement, the relationship between changing radiative heating and vertical air motion, is very similar. Both regions indicate the condensational cooling/heating profile from the NoS case with LW cooling at middle levels (700 hPa) and aloft near the cloud top (300 hPa). The compensating moist condensational heating is associated with the ascending motions above 650 hPa whereas the condensational cooling (rain reevaporative cooling) is associated with the descending motions below 650 hPa. The low-level descending over the ITCZ is accompanied by low-level wind divergence at 850 hPa shown in Figures 8f and 9e. The warm pool regions contain many land-covered regions involving complicated land surface processes. However, we include two profiles in the warm pool shown in Figures 10c and 10d from the regions. The changing of upper level longwave radiative cooling and vertical air motion is very similar to the profiles over ITCZ shown in Figures 10a and 10b. Compared to the regions over ITCZ, both regions indicate much stronger condensational cooling/heating profile from the NoS case along with the larger ascending motions above 600 hPa and descending motions below 600 hPa.

There is a remarkable resemblance between the biases of YOTC-GASS GCMs in low-level winds, surface precipitation and 500 hPa moisture and the difference between the NoS and S cases (cf. Figure 6a with Figure 9e, Figure 6b with Figure 9f, and Figure 6c with Figure 9g). Such resemblance suggests that the above mentioned physical processes responsible for the differences between NoS and S experiments are applicable to explain the biases in uncoupled YOTC-GASS GCMs. That is, the local low-level wind convergence (Figure 6a) is a consequence of stronger local large-scale ascending motion near the southern part of the ITCZ and the northern edge of the SPCZ. The low-level southeastward and eastward wind anomalies result in greater warm/moist air advection along the belt of 5°N–10°S and 150°E–120°W (not shown) and increased precipitation (Figure 6b).

4.4. Biases of Vertical Structure of Radiation in NCAR CESM1

Previous section underscores the role of snow-radiative effects in the dynamics of the uncoupled CESM1. Here we investigate its role in the coupled system in the CESM1, with a focus on the changes and biases in
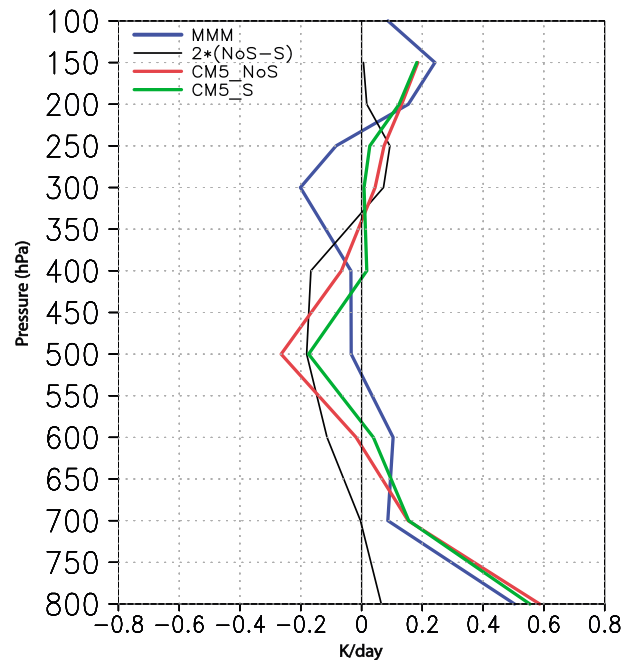
Figure 12. Annual mean biases in longwave radiative heating rates against CloudSat-CALIPSO-derived 2B-FLXHR-LIDAR radiative heating rates (unit: K d^{-1}) in the Pacific trade wind region [30°S–0°N; 180°E–80°W] for the NoS case (red), the S case (green) and the MMM from the YOTC-MJO Task Force (blue). The difference between NoS and S by a factor of 2 is shown in black.

the vertical structure of LW radiative heat rates in the Pacific sector. It is shown that the biases of both uncoupled and coupled runs share similar spatial characteristics that LW radiative cooling is apparent in the levels of 450–550 hPa across the tropical zone (~30°S to ~30°N) and maximizes near 500 hPa (Figures 11a, 11b, 11d, and 11e). Regardless of uncoupled and coupled runs, the biases of LW radiative cooling for the S cases are reduced from their NoS counterparts by about 10~15% (Figures 11c and 11f).

Figure 12 shows the annual mean biases of LW radiative cooling rates for the coupled NoS case (red), the S case (green), and their difference by the factor of 2 (black), as well as the MMM from YOTC-GASS (blue) in the Pacific trade wind region [30°S–0°N; 180°E–80°W] against 2B-FLXHR-LIDAR. It is evident that the NoS case produces more LW cooling that would trigger more convective instability in the lower and middle level troposphere. The inclusion of the snow radiative effect helps reduce the cooling bias of the NoS case by 10–15%.

5. Summary

Previous studies indicated that most GCMs in CMIP3 and CMIP5 represent the floating cloud mass in the atmospheric column that resides in clouds but typically do not represent falling particles (such as snow and rain) and convective core mass—including their interaction with radiation [e.g., *Li et al.*, 2013, 2014a; *Waliser et al.*, 2009]. Unlike most GCMs, observation-based products, including *CloudSat* and CALIPSO and SW/LW radiative heating rates and fluxes (CloudSat-CALIPSO-derived 2B-FLXHR-LIDAR), are sensitive to not only small cloud ice particles but large falling precipitating particles. The comparison between models and observations revealed the systematic biases of the radiation budget in the multimodel examination of AMIP5 and CMIP5 simulations, which are consequences of a significant underestimation of the total ice water path [*Li et al.*, 2013]. Without the consideration of large falling precipitating (and/or convective core) particles on radiation, an overestimation of RLUT and RSDS is present in the strongly convective and precipitating regions (i.e., western Pacific, ITCZ/SPCZ, tropical landmass, and storm tracks) [*Li et al.*, 2013].

A series of comprehensive studies identified the time-mean biases in radiation, dynamical variables, and oceanic state properties for CMIP3 and CMIP5 models and attributed the nontrivial biases in part to the absence of snow-radiation effects. However, the missing vertical radiative heating output in CMIP3 and CMIP5 models has left the impacts of the snow-radiation on dynamical interactions between vertical motions and condensation heating unclear.

This study provides a comprehensive examination and discussion on the cloud snow radiative effect in an aspect of radiative heating profiles in both uncoupled and coupled systems. We focus on the link of the vertical radiative heating rates to the simulated compensating condensational heating, cloud LW radiative cooling rates, water vapor, horizontal winds, and vertical velocity in the Pacific sector. We begin with the comparison of the RLUT biases between the YOTC-GASS GCMs, the AMIP5, and CMIP5 models, displaying consistency especially over the subtropical and the tropical Pacific regions. The model outputs from the YOTC-GASS GCMs can not only represent the features of biases in CMIP models but offer the vertical profiles of radiative heating. We find pronounced radiative cooling bias in the upper troposphere between 30°S and

30°N in the YOTC-GASS GCMs relative to observations and aim for investigating the role of the snow-radiation effect in this cooling bias with the help of sensitivity experiments in the NCAR CESM1. By excluding the snow-radiative effects, the uncoupled CESM1 simulations indicate too much downward SW radiation at the surface and excessive upward LW radiation at TOA (~up to 15 W m^{-2}) in strongly precipitating/convective regions over ITCZ/SPCZ and warm pool. There is approximately 10–15% excessive cooling for NoS relative to S at middle to just below cloud top in the upper tropospheric levels (Figure 11). This vertically destabilizing LW radiative cooling tends to generate unstable columns and trigger stronger convection with enhanced updraft and downdraft. This results in ascending motion aloft with condensational heating and descending in the middle and lower troposphere with condensational cooling. The anomalous upper level vertical motion is accompanied by the low-level descending motion-associated stronger convective downdraft resulting in low-level divergence over ITCZ/SPCZ and warm pool. These effective low-level outflow anomalies, against trade winds, eastward and/or southeastward advection from the warm pool, and ITCZ/SPCZ, lead to moist/warm convergence in conjunction with excessive precipitation and columnar water vapor in the SPCZ, ITCZ, and the regions between the edges and trade wind regions north of the ITCZ. The improvement of the vertical LW radiative cooling profiles holds true when the coupled CESM1 considers the presence of the snow-radiation effect.

In this study, we isolate the contributions from the ocean-related processes with uncoupled CESM1 experiments. Our results suggest that the interaction between atmospheric dynamics and radiative fields is a significant contributor to the biases in column excessive water vapor, excessive surface precipitation in subtropical Pacific oceans shown in the YOTC-GASS, and the uncoupled CESM1. Different from the uncoupled CESM1, the contributor to excessive precipitation and too moist subtropical Pacific in the coupled GCMs is the combining effect of the warmer SSTs associated with weaker upper ocean mixing in the subtropical oceans and the effective warm and moist advections in the atmosphere [*Li et al.*, 2014a, 2015]. Although we cannot conclude that all of the biases in the GCMs arise from the exclusion of the snow-radiation effects, we cannot ignore the contribution of these effects make in many aspects of the coupled and uncoupled climate systems, such as the atmospheric and ocean circulations in coupled GCMs.

6. Discussion

Before the CloudSat-CALIPSO data availability in June 2006, a key element of obtaining an accurate top of atmosphere (TOA) and surface radiation budget is the representation of clouds, which for GCMs and earth radiation budget considerations can be roughly broken down into *cloud cover*, *cloud water mass*, and *cloud particle sizes*. Most conventional GCMs, such as CMIP3/CMIP5, only represent floating cloud ice radiative effects, ignoring precipitating cloud radiative forcing (snow and rain), using passive measurements such as MODIS, Earth Radiation Budget Experiment, International Satellite Cloud Climatology Project, and other products have provided some very useful information for the constraints on cloud cover. However, the latter two quantities, cloud mass, and their sizes, have been largely unconstrained due to the lack of observations for vertical structure of cloud water mass and particle size, leaving too many degrees of freedom unconstrained. The ramifications of this issue for cloud mass is clearly evident in the wide disparity in the cloud ice and liquid water content (CIWC and CLWC) values exhibited in present-day models, including those contributing to Phases 3 and 5 of the Coupled Model Intercomparison Project (CMIP3 and CMIP5) [e.g., *Li et al.*, 2012]. For example, in *Li et al.* [2012], they have shown that the snow contributes almost 2/3 of the total ice mass distributions in terms of ice water content (IWC) and path (IWP) illustrated in Figures 1, 3, 5a, and 8 from their paper.

Li et al. [2013] documented that most of the conventional GCMs (e.g., CMIP3 and CMIP5 models) consider radiation interactions only with suspended cloud mass, ignoring falling ice snow mass. Nevertheless, constraints on models' global radiation balance, clouds, and related quantities are made with measurements (e.g., CloudSat Radar and the Clouds and the Earth's Radiant Energy System (CERES) [*Wielicki et al.*, 1996]) sensitive to the *broader range of hydrometeors* that include suspended small cloud particles and precipitating hydrometeors [*Li et al.*, 2011, 2012; *Waliser et al.*, 2009]. Thus, most of the GCMs in CMIP3 and CMIP5 are likely to contain either significant error and/or incorrectly partition of the cloud hydrometeor populations, which may result in further biases in the radiation fields [*Li et al.*, 2013]. This has been further supported by *Li et al.* [2013], who found the same persistent systematic biases in CMIP3 and CMIP5 (compared to

observations), noting that these biases occur in conjunction with a significant underestimation of the ice water content/path (IWC/IWP) [see *Li et al.*, 2012, Figures 5a and 8].

From the above mentioned discussion, it is one of the reasons why, in general, global or zonal averages of the "net radiation budget," OLR and SW radiation budgets might potentially be able to be removed globally by tuning. The local biases, however, in the cases of snow dominate regions (ITCZ, SPCZ, etc.), might be able to be removed for net radiation budget (which is commonly used in most tuning) through cancelation between OLR (outgoing) and SW (incoming) but might not be able to be removed for individual OLR and SW radiation biases even by the elaborated tunings.

It is important to note that, however, we cannot conclude that all of the radiation biases in the current GCMs are due to the exclusion of the snow-radiation effects. We cannot ignore the contribution of many other the cloud-radiation related biases in a GCM [e.g., *Jakob*, 2002; *Iga et al.*, 2011], for example, the horizontal coverage of cloud fraction, the vertical extent of the clouds, the particle size and shape, and their falling speed as well as the sources and sinks of cloud condensate (and their radiative properties) including condensation, evaporation/sublimation, conversion into precipitation and fallout [*Iga et al.*, 2011], etc.

References

Austin, R., and G. L. Stephens (2001), Retrieval of stratus cloud microphysical parameters using millimeter-wave radar and visible optical depth in preparation for CloudSat: 1. Algorithm formulation, *J. Geophys. Res.*, *106*, 28,233–28, 242, doi:10.1029/2000JD000293.

Austin, R. T., A. J. Heymsfield, and G. L. Stephens (2009), Retrieval of ice cloud microphysical parameters using the CloudSat millimeter-wave radar and temperature, *J. Geophys. Res.*, *114*, D00A23, doi:10.1029/2008JD010049.

Bao, Q., et al. (2013), The Flexible Global Ocean-Atmosphere-Land system model, Spectral version 2: FGOALS-s2, *Adv. Atmos. Sci.*, *30*, 561–576.

Côté, J., S. Gravel, A. Méthot, A. Patoine, M. Roch, and A. Staniforth (1998), The Operational CMC–MRB Global Environmental Multiscale (GEM) Model. Part I: Design Considerations and Formulation, *Mon. Weather Rev.*, *126*, 1373–1395.

Dee, D. P., and S. Uppala (2009), Variational bias correction of satellite radiance data in the ERA-Interim reanalysis, *Q. J. R. Meteorol. Soc.*, *135*, 1830–1841, doi:10.1002/qj.493.

Fetzer, E. J., et al. (2008), Comparison of upper tropospheric water vapor observations from the Microwave Limb Sounder and Atmospheric Infrared Sounder, *J. Geophys. Res.*, *113*, D22110, doi:10.1029/2008JD010000.

Forbes, R., A. Tompkins, and A. Untch (2012), A new prognostic bulk microphysics scheme for the IFS, ECMWF Tech. Memo 649.

Gettelman, A., X. Liu, S. J. Ghan, H. Morrison, S. Park, A. J. Conley, S. A. Klein, J. Boyle, D. L. Mitchell, and J.-L. F. Li (2010), Global simulations of ice nucleation and ice supersaturation with an improved cloud scheme in the Community Atmosphere Model, *J. Geophys. Res.*, *115*, D18216, doi:10.1029/2009JD013797.

Haynes, J. M., T. S. L'Ecuyer, G. L. Stephens, S. D. Miller, C. Mitrescu, N. B. Wood, and S. Tanelli (2009), Rainfall retrieval over the ocean with spaceborne W-band radar, *J. Geophys. Res.*, *114*, D00A22, doi:10.1029/2008JD009973.

Hazeleger, W., et al. (2012), EC-Earth V2.2: Description and validation of a new seamless earth system prediction model, *Clim. Dyn.*, *39*, 2611–2629.

Henderson, D. S., T. L'Ecuyer, G. Stephens, P. Partain, and M. Sekiguch (2013), A multi-sensor perspective on the radiative impacts of clouds and aerosols, *J. Appl. Meteorol. Climatol.*, *52*, 852–870.

Hogan, T. F., et al. (2012), Exposing global cloud biases in the Community Atmosphere Model (CAM) using satellite observations and their corresponding instrument simulators, *J. Clim.*, *25*, 5190–5207, doi:10.1175/JCLI-D-11-00469.1.

Huffman, G. J., R. F. Adler, P. Arkin, A. Chang, R. Ferraro, A. Gruber, J. Janowiak, A. McNab, B. Rudolf, and U. Schneider (1997), The Global Precipitation Climatology Project (GPCP) combined precipitation dataset, *Bull. Am. Meteorol. Soc.*, *78*, 5–20.

Iga, S., H. Tomita, Y. Tsushima, and M. Satoh (2011), Sensitivity of upper tropospheric ice clouds and their impacts on the Hadley circulation using a global cloud-system resolving model, *J. Clim.*, *24*, 2666–2679.

Jakob, C. (2002), Ice clouds in numerical weather prediction models: Progress, problems, and prospects, in *Cirrus*, edited by D. K. Lynch et al., pp. 327–345, Oxford Univ. Press.

Jiang, X., et al. (2015), Vertical structure and physical processes of the Madden-Julian Oscillation: Exploring key model processes in climate simulations, *J. Geophys. Res. Atmos.*, *120*, 4718–4748, doi:10.1002/2014JD022375.

Lappen, C.-L., and C. Schumacher (2012), Heating in the tropical atmosphere: What level of detail is critical for accurate MJO simulations in GCMs?, *Clim. Dyn.*, *39*, 2547–2568.

L'Ecuyer, T. S., N. Wood, T. Haladay, and G. L. Stephens (2008), The impact of clouds on atmospheric heating based on the R04 CloudSat fluxes and heating rate detest, *J. Geophys. Res.*, *113*, D00A15, doi:10.1029/2008JD009951.

Li, J.-L. F., D. Waliser, C. Woods, J. Teixeira, J. Bacmeister, J. Chern, B.-W. Shen, A. Tompkins, W.-K. Tao, and M. Köhler (2008), Comparisons of satellites liquid water estimates to ECMWF and GMAO analyses, 20th century IPCC AR4 climate simulations, and GCM simulations, *Geophys. Res. Lett.*, *35*, L19710, doi:10.1029/2008GL035427.

Li, J.-L. F., D. E. Waliser, and J. H. Jiang (2011), Correction to "Comparisons of satellites liquid water estimates to ECMWF and GMAO analyses, 20th century IPCC AR4 climate simulations, and GCM simulations", *Geophys. Res. Lett.*, *38*, L24807, doi:10.1029/2011GL049956.

Li, J.-L. F., et al. (2012), An observationally-based evaluation of cloud ice water in CMIP3 and CMIP5 GCMs and contemporary analyses, *J. Geophys. Res.*, D16105, doi:10.1029/2012JD017640.

Li, J.-L. F., D. E. Waliser, G. Stephens, S. Lee, T. L'Ecuyer, S. Kato, N. Loeb, and H.-Y. Ma (2013), Characterizing and understanding radiation budget biases in CMIP3/CMIP5 GCMs, contemporary GCM, and reanalysis, *J. Geophys. Res. Atmos.*, *118*, 8166–8184, doi:10.1002/jgrd.50378.

Li, J.-L. F., W.-L. Lee, D. E. Waliser, J. David Neelin, J. P. Stachnik, and T. Lee (2014a), Cloud-precipitation-radiation-dynamics interaction in global climate models: A snow and radiation interaction sensitivity experiment, *J. Geophys. Res. Atmos.*, *119*, 3809–3824, doi:10.1002/2013JD021038.

Li, J.-L. F., W.-L. Lee, D. E. Waliser, J. P. Stachnik, E. Fetzer, S. Wong, and Q. Yue (2014b), Characterizing tropical Pacific water vapor and radiative biases in CMIP5 GCMs: Observation-based analyses and a snow and radiation interaction sensitivity experiment, *J. Geophys. Res. Atmos.*, 119, 10,981–10,995, doi:10.1002/2014JD021924.

Li, J.-L. F., R. M. Forbes, D. E. Waliser, G. Stephens, and S. W. Lee (2014c), Characterizing impacts of precipitating snow hydrometeors in the radiation using the ECMWF IFS global model, *J. Geophys. Res. Atmos.*, 119, doi:10.1002/2014JD021450.

Li, J.-L. F., W.-L. Lee, T. Lee, E. Fetzer, and J.-Y. Yu (2015), The impacts of cloud snow radiative effects on pacific oceans surface heat fluxes, surface wind stress, and ocean temperatures in coupled GCM simulations, *J. Geophys. Res. Atmos.*, 120, 2242–2260, doi:10.1002/2014JD022538.

Lindvall, J., G. Svensson, and C. Hannay (2013), Evaluation of near-surface parameters in the two versions of the atmospheric model in CESM1 using flux station observations, *J. Clim.*, 26, 26–44, doi:10.1175/JCLI-D-12-00020.1.

Liou, C. S., J. H. Chen, C. T. Terng, F. J. Wang, C. T. Fong, T. E. Rosmond, H. C. Kuo, C. H. Shiao, and M. D. Cheng (1997), The second–generation global forecast system at the central weather bureau in Taiwan, *Weather Forecasting*, 12, 653–663.

Loeb, N. G., B. A. Wielicki, D. R. Doelling, G. L. Smith, D. F. Keyes, S. Kato, N. Manalo-Smith, and T. Wong (2009), Toward optimal closure of the Earth's top-of-atmosphere radiation budget, *J. Clim.*, 22(3), 748–766.

Loeb, N. G., J. M. Lyman, G. C. Johnson, R. P. Allan, D. R. Doelling, T. Wong, B. J. Soden, and G. L. Stephens (2012), Observed changes in top-of-the-atmosphere radiation and upper-ocean heating consistent within uncertainty, *Nat. Geosci.*, 5, 110–113, doi:10.1038/NGEO1375.

Merryfield, W. J., W.-S. Lee, G. J. Boer, V. V. Kharin, J. F. Scinocca, G. M. Flato, R. S. Ajayamohan, J. C. Fyfe, Y. Tang, and S. Polavarapu (2013), The Canadian seasonal to interannual prediction system. Part I: Models and initialization, *Mon. Weather Rev.*, 141, 2910–2945.

Molod, A., L. Takacs, L. M. Suarez, J. Bacmeister, I.-S. Song, and A. Eichmann (2012), The GEOS-5 atmospheric general circulation model: Mean climate and development from MERRA to Fortuna, NASA Tech. Rep. Series on Global Modeling and Data Assimilation, NASA TM-2012-104606, Vol. 28, 117 pp.

Morrison, H., and A. Gettelman (2008), A new two-moment bulk stratiform cloud microphysics scheme in the NCAR Community Atmosphere Model (CAM3), Part I: Description and numerical tests, *J. Clim.*, 21, 3642–3659.

Neale, R. B., et al. (2012), Description of the NCAR Community Atmosphere Model: CAM 5.0, *Tech. Rep. NCAR/TN-486 + STR*, 274 pp., Natl. Cent. for Atmos. Res., Boulder, Colo.

Olsen, E. T., et al. (2013), AIRS/AMSU/HSB version 6 level 2 product user guide, Version 1.01. Jet Propul. Lab./Calif. Inst. of Technol., Pasadena, Calif.

Petch, J., D. Waliser, X. Jiang, P. Xavier, and S. Woolnough (2011), A global model intercomparison of the physical processes associated with the MJO, *WCRP GEWEX News*, 21(3), 3–5.

Randall, D. A., et al. (2007), Climate models and their evaluation, in *Climate Change 2007: The Physical Science Basis. Contribution of Working Group I to the Fourth Assessment Report of the Intergovernmental Panel on Climate Change*, edited by S. Solomon et al., pp. 589–662, Cambridge Univ. Press, Cambridge, U. K.

Schmidt, G. A., et al. (2014), Configuration and assessment of the GISS ModelE2 contributions to the CMIP5 archive, *J. Adv. Model. Earth Syst.*, 6, 141–184, doi:10.1002/2013MS000265.

Song, X., G. J. Zhang, and J.-L. F. Li (2012), Evaluation of microphysics parameterization for convective clouds in the NCAR Community Atmosphere Model CAM5, *J. Clim.*, 25, 8568–8590, doi:10.1175/JCLI-D-11-00563.1.

Stan, C., M. Khairoutdinov, C. A. DeMott, V. Krishnamurthy, D. M. Straus, D. A. Randall, J. L. Kinter III, and J. Shukla (2010), An ocean-atmosphere climate simulation with an embedded cloud resolving model, *Geophys. Res. Lett.*, 37, L01702, doi:10.1029/2009GL040822.

Stephens, G. L. (2005), Cloud feedbacks in the climate system: A critical review, *J. Clim.*, 18, 237–273.

Stevens, B., et al. (2013), Atmospheric component of the MPI-M Earth System Model: ECHAM6, *J. Adv. Model. Earth Syst.*, 5, 146–172, doi:10.1002/jame.20015.

Takemura, T., T. Nakajima, O. Dubovik, B. N. Holben, and S. Kinne (2002), Single-scattering albedo and radiative forcing of various aerosol species with a global three-dimensional model, *J. Clim.*, 15, 333–352.

Taylor, K. E., R. J. Stouffer, and G. A. Meehl (2012), An overview of CMIP5 and the experiment design, *Bull. Am. Meteorol. Soc.*, 93, 485–498.

Tian, B., E. Manning, E. Fetzer, E. Olsen, and S. Wong (2013b), AIRS/AMSU/HSB version 6 level 3 product user guide, Version 1.01. Jet Propul. Lab./Calif. Inst. of Technol.

Voldoire, A., et al. (2013), The CNRM-CM5.1 global climate model: Description and basic evaluation, *Clim. Dyn.*, 40, 2091–2121.

Waliser, D. E., et al. (2009), Cloud ice: A climate model challenge with signs and expectations of progress, *J. Geophys. Res.*, 114, D00A21, doi:10.1029/2008JD010015.

Waliser, D. E., J.-L. F. Li, T. S. L'Ecuyer, and W.-T. Chen (2011), The impact of precipitating ice and snow on the radiation balance in global climate models, *Geophys. Res. Lett.*, 38, L06802, doi:10.1029/2010GL046478.

Walters, D. N., et al. (2011), The Met Office Unified Model Global Atmosphere 3.0/3.1 and JULES Global Land 3.0/3.1 configurations, *Geosci. Model Dev.*, 4, 919–941.

Watanabe, M., et al. (2010), Improved climate simulation by MIROC5: Mean states, variability, and climate sensitivity, *J. Clim.*, 23, 6312–6335.

Wielicki, B. A., B. R. Barkstrom, E. F. Harrison, R. B. Lee, G. L. Smith, and J. E. Cooper (1996), Clouds and the Earth's Radiant Energy System (CERES): An Earth observing system experiment, *Bull. Am. Meteorol. Soc.*, 77, 853–868.

Wu, T., R. Yu, F. Zhang, Z. Wang, M. Dong, L. Wang, X. Jin, D. Chen, and L. Li (2010), The Beijing Climate Center atmospheric general circulation model: Description and its performance for the present-day climate, *Clim. Dyn.*, 34, 123–147.

Wu, X., and L. Deng (2013), Comparison of moist static energy and budget between the GCM-simulated Madden–Julian oscillation and observations over the Indian Ocean and Western Pacific, *J. Clim.*, 26, 4981–4993.

Yukimoto, S., et al. (2012), A new global climate model of the Meteorological Research Institute: MRI-CGCM3-model description and basic performance, *J. Meteorol. Soc. Jpn. Ser. II*, 90A, 23–64.

Zhang, G. J., and M. Mu (2005), Simulation of the Madden-Julian oscillation in the NCAR CCM3 using a revised Zhang-McFarlane convection parameterization scheme, *J. Clim.*, 18, 4046–4064.